Relationship between bubble generation behavior and hydrogen evolution reaction performance at high current densities during alkaline water electrolysis

Daisuke Kitajima [a], Ryuta Misumi [b,c,*], Yoshiyuki Kuroda [b,c], Shigenori Mitsushima [b,c]

[a] *Department of Chemistry and Life Science, Graduate School of Engineering Science, Yokohama National University, 79-5 Tokiwadai, Hodogaya-ku, Yokohama, Kanagawa 240-8501, Japan*

[b] *Division of Materials and Chemical Engineering, Faculty of Engineering, Yokohama National University, 79-5 Tokiwadai, Hodogaya-ku, Yokohama, Kanagawa 240-8501, Japan*

[c] *Advanced Chemical Energy Research Center, Institute of Advanced Sciences, Yokohama National University, 79-5 Tokiwadai, Hodogaya-ku, Yokohama, Kanagawa 240-8501, Japan*

ARTICLE INFO

ABSTRACT

Alkaline water electrolysis (AWE) has attracted considerable attention in recent years as a means to produce hydrogen. However, one problem associated with AWE is the increase in overpotential at high current densities, which is attributed to bubble coverage on the electrode surface. It is therefore important to understand the bubble generation behavior to ultimately reduce the overpotential. In this study, a method was established to measure the resistance components from the electrolytic reaction and bubble coating separately based on the use of electrochemical impedance spectroscopy. The results were related to the bubble generation behavior on a Ni electrode, as observed using a high-speed camera. Consequently, a model for the degradation of the electrolytic efficiency due to bubble generation was devised, and the effect of the bubble coverage layer was quantitatively evaluated.

1. Introduction

Renewable energy is important for realizing carbon neutrality. However, the electricity generated from renewable energy sources such as wind and solar power is unevenly distributed in places far from cities, its output is unstable, and there is often a mismatch between generation and demand. To address these issues, alkaline water electrolysis (AWE) has been developed to effectively convert electrical power into hydrogen, which is easily stored. AWE is particularly advantageous due to the fact that it can employ non-precious metals, such as Ni, as the catalyst. In addition, its simple configuration renders device scale-up relatively facile. However, this technique only delivers a high efficiency at low current densities ($\leq$0.6 A cm^{-2}), and so there is a requirement to address this issue and provide devices that function under practical current densities [1,2].

One of the challenges in achieving highly efficient AWE is that at high current densities, the electrode surface is covered by microbubbles,

which are generated during the reaction, thereby reducing the electrolysis efficiency [3,4]. Indeed, at current densities of ~0.7 A cm^{-2}, this bubble effect can no longer be ignored [5]. To date, various reports have described the direct observation of bubbles on the electrode surface [5–8], while others have approached the mechanism of bubble detachment from the electrode from a dynamic point of view [9,10]. It has been reported that the apparent electrical conductivity of the electrolyte decreases and the ohmic resistance increases owing to the passage of ions, which carry charges around the non-conductive bubbles [5,11,12]. In general, the maximum current density of an electrochemical reaction is significantly affected by the limitations of reactant mass transfer [13]; therefore, the influence of bubble generation on mass transfer must be properly assessed in electrolytic processes.

In terms of the oxygen evolution reaction (OER), it has been reported that bubble coverage on the electrode can restrict ionic mass transfer; consequently, diffusion resistance appears in addition to ohmic resistance [5]. A model in which a dual-bubble coverage layer is formed on the electrode surface has been devised, and the effect of the bubbles has

---

Nomenclature

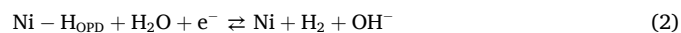|	
C_{bub}	Capacitance due to bubble coverage, modeled by capacitive semicircles (F cm^{-2})
D_{WE}	Cross-sectional diameter of the working electrode (cm)
E	Measured electrode potential (V vs. RHE)
$E_{iR\ free}$	Electrode potential after solution resistance correction (V vs. RHE)
f	EIS frequency (Hz)
i_{geo}	Current density normalized by the geometrical surface area (A cm^{-2})
$Im(Z)$	Imaginary axis of the Cole–Cole plot (Ω cm^2)
L	Length of the exposed horizontal section of the electrode (cm)
L_1	Inductance modeled by inductive semicircles in the high frequency range (L cm^{-2})
L_2	Inductance modeled by inductive semicircles in the medium frequency range associated with H$_{OPD}$ adsorption (L cm^{-2})
L_3	Inductance modeled by inductive semicircles in the low-frequency range owing to accelerated bubble detachment (L cm^{-2})
Q_{dl}	Capacitance modeled by CPE (constant phase element) corresponding to the electrical double layer (F cm^{-2})
R_{bub}	Diffusion resistance due to bubble coverage, modeled by capacitive semicircles (Ω cm^2)
R_{ct}	Charge-transfer resistance (Ω cm^2)
R_d	Diffusion resistance in the inner bubble layer at the anode (Ω cm^2)
$Re(Z)$	Real axis of the Cole–Cole plots (Ω cm^2)
R_{L1}	Resistance modeled by the inductive semicircle in the high frequency range (Ω cm^2)
R_{L2}	Negative resistance associated with H$_{OPD}$ adsorption, modeled by the inductive semicircle in the medium frequency range (Ω cm^2)
R_{L3}	Negative resistance induced by accelerated bubble detachment, modeled by inductive semicircle in the low frequency range (Ω cm^2)
R_{p1}	Apparent charge-transfer resistance due to R_{ct} and R_{L2} (Ω cm^2)
R_{p2}	Apparent diffusion resistance due to R_{bub} and R_{L3} in the bubble coverage layer (Ω cm^2)
R_{s0}	Solution resistance in the bulk (Ω cm^2)
R_{sb}	Incremental solution resistance in the bubble coverage layer (Ω cm^2)
S_{bubble}	Logarithmic mean of the geometrical electrode surface area and the outer surface area of the bubble layer (cm^2)
S_{geo}	Geometrical electrode surface area (cm^2)
x	Constant of the Bruggeman equation (−)
$\|Z\|$	Impedance in the Bode diagram (Ω cm^2)
δ_b	Thickness of the bubble layer (cm)
ε	Void fraction of the bubble layer (−)
$\Delta\eta$	Overvoltage from the theoretical decomposition voltage (V)
θ	Phase angle in the Bode diagram (°)
κ	Electrical conductivity of the electrolyte (S m^{-1})

been modeled as an increase in the solution resistance caused by migration of the OH$^-$ charge carriers between gaps in the bubble layer and an increase in resistance due to diffusion of the reactant OH$^-$ ions [5,14,15].

During the hydrogen evolution reaction (HER) of AWE, two types of hydrogen atoms are adsorbed on the metal electrode surface: H$_{OPD}$ (hydrogen atoms adsorbed at a more negative potential than the theoretical decomposition potential of the HER (i.e., overpotential deposition, OPD)) and H$_{UPD}$ (hydrogen atoms adsorbed at a higher (more positive) potential than the theoretical decomposition potential of the HER (i.e., underpotential deposition, UPD)). H$_{OPD}$ are considered to be intermediates of the HER, whereas H$_{UPD}$ form stronger bonds with metals than H$_{OPD}$, and so are not considered intermediates [16,17]. However, it has been reported that H$_{UPD}$ can accelerate the HER [18]. In general, under alkaline conditions, the HER involves three reactions [19–21]:
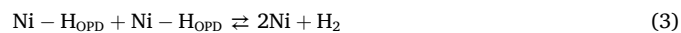
Volmer reaction:

$$Ni + H_2O + e^- \rightleftarrows Ni - H_{OPD} + OH^- \tag{1}$$

Heyrovsky reaction:

$$Ni - H_{OPD} + H_2O + e^- \rightleftarrows Ni + H_2 + OH^- \tag{2}$$

Tafel reaction:

$$Ni - H_{OPD} + Ni - H_{OPD} \rightleftarrows 2Ni + H_2 \tag{3}$$
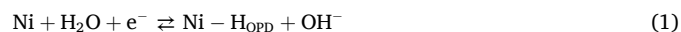
In the first stage, namely the Volmer reaction (Eq. (1)), the bonds between the hydrogen and oxygen atoms of the water molecules are broken, and the hydrogen atoms are chemisorbed onto the metal electrode surface. These adsorbed hydrogen atoms then generate H$_2$ through the Heyrovsky reaction (Eq. (2)) or the Tafel reaction (Eq. (3)). In the Heyrovsky reaction, the adsorbed hydrogen atoms react with water to form H$_2$, whereas in the Tafel reaction, H$_2$ is formed by the direct combination of two adsorbed hydrogen atoms. In general, the HER is considered to proceed mainly via the Volmer–Heyrovsky process.

It is generally accepted that the rate-limiting step is the Tafel reaction when the value of the Tafel slope is 30 mV dec^{-1}, the Heyrovsky reaction when the slope is 40 mV dec^{-1}, and the Volmer reaction when the slope is 120 mV dec^{-1} [19]. However, according to some electrolytic simulation results [20,21], the Heyrovsky reaction can be the rate-limiting step even with a Tafel slope of 120 mV dec^{-1}. More specifically, when hydrogen atoms are present in abundance on the electrode surface, their adsorption approaches a constant value upon varying the current density, and the Tafel slope does not contain enough information to determine the rate-limiting step [20,21]. It has also been reported that the hydrogen adsorption rate θ_H is close to 0 when the initial Volmer reaction is rate-limiting, whereas it is close to 1 when the Heyrovsky reaction is rate-limiting. It has been suggested that the rate-limiting step of the HER can be determined by measuring the amount of adsorbed H$_{OPD}$ [16,20,21]. Indeed, the detection of abundant H$_{OPD}$ species has been reported at higher potentials where few hydrogen bubbles are produced [22], thereby suggesting that the rate-limiting step of the HER is the Heyrovsky reaction [16].

Simulations have shown the presence of two capacitive semicircles (with corresponding charge-transfer resistances of 40 and 120 mV dec^{-1}) in the Cole–Cole plots when the Heyrovsky reaction is the rate-limiting step. As the potential becomes more negative, the size relationship between the two semicircles is reversed, leading to a transition of the Tafel slope from 40 to 120 mV dec^{-1} [21]. This phenomenon of two capacitive semicircles in the transition zone of the Tafel slope has also been described in experimental reports [22,23], further suggesting that the rate-limiting step of the HER is the Heyrovsky reaction.

With respect to hydrogen bubble generation behavior at the cathode, it has been reported that the hydrogen bubble diameter decreases with increasing current density in the small current density range. This is thought to be due to an increase in the nucleation rate with increasing current density [24]. It has also been found that the hydrogen bubble diameter and the hydrogen overvoltage decrease at increased KOH concentrations [9,24]. However, few studies have discussed the effects

of bubbles on the overvoltage at high current densities from a mass transfer perspective.

In this study, focusing on the HER at high current densities where hydrogen bubbles cover the electrode surface, the influence of bubble generation on the HER performance is quantitatively evaluated by observing the electrode surface with a high-speed video camera system and using electrochemical impedance spectroscopy (EIS). An equivalent circuit model is used to separate the resistance components (i.e., charge-transfer resistance, ohmic resistance, and diffusion resistance) at each current density and quantify each resistance based on its origin, such as electrolytic reactions (Heyrovsky reaction) or bubbles. By combining the Cole–Cole plot results with high-speed video footage of the bubble formation and bubble coverage layer, a model is proposed to clarify the phenomena corresponding to each of the resistance components at each current density. Finally, the effect of the electrode diameter on the electrolytic performance is evaluated and compared with the anodic reaction model.

2. Experimental

2.1. Experimental setup

Figure S1 shows a schematic diagram of the three-electrode cell prepared herein. More information on this setup is given in our previous reports [5,6]. The electrolyte solution was 2 M KOH solution at a temperature of 30 ± 1 °C (controlled using an external heat exchanger and a tube pump). The working electrode consisted of a cylindrical Ni wire with a diameter of 150, 200, or 300 μm (>99% purity, Nilaco Corporation, Japan). The counter and reference electrodes consisted of bare Ni rods (3 mm diameter each, total 8 rods) and a reversible hydrogen electrode (RHE), respectively. To ensure a homogeneous current density distribution, four counter electrodes were placed on each side of the cell at an equal distance from the working electrode. The working electrode was ultrasonically cleaned in a 1 M hydrochloric acid solution for 1 min, and then coated with epoxy resin and polytetrafluoroethylene heat-shrinkable tubes. A horizontal section of the electrode (~3 mm) was left exposed to observe bubble generation, and vertical section of it was covered by epoxy resin. The distance between the working electrode and the Luggin capillary of the RHE was set to ~2 mm using a micro-traverse machine to minimize the solution resistance and prevent bubbles from contacting the Luggin capillary. For the purpose of this study, the current density i_{geo} (A cm^{-2}) was normalized by the geometric surface area of the working electrode, S_{geo} (cm^2), which is expressed as follows:

$$S_{geo} = \pi D_{WE} L \tag{4}$$

where D_{WE} (cm) is the diameter of the working electrode and L (cm) is the length of the exposed horizontal section. N$_2$ gas was flowed through the system during the electrochemical measurements to minimize the effects of any dissolved gasses.

2.2. Electrochemical measurement conditions

Electrochemical measurements were performed using an SP-150 electrochemical measurement system (BioLogic Science Instruments, Ltd., France). To stabilize the electrode active state, cyclic voltammetry (CV) was carried out for 1000 cycles between −0.3 and −1.0 V vs. RHE (scan rate = 20 mV s^{-1}). After pretreatment, CV was performed for five cycles over the same voltage range (scan rate = 5 mV s^{-1}), and the HER performance was evaluated based on the polarization curve recorded for the fifth cycle. The solution resistance at a measured electrode potential E of −0.4 V vs. RHE, i.e., the point at which the polarization curve follows the Tafel slope and the effect of bubbles was small, was defined as the solution resistance in the bulk (R_{s0}, Ω cm^2). A correction for iR was performed using Eq. (5):

$$E_{iR\ free} = E - i_{geo}R_{s0@-0.4\ V\ vs.\ RHE} \tag{5}$$

where $E_{iR\ free}$ (V vs. RHE) is the electrode potential after solution resistance correction and i_{geo} (A cm^{-2}) is the measured current density. Slightly poorer performance was observed for the anodic scans (Fig. S2), where the difference between the EIS and CV results was smaller with respect to the relationship between the current and potential. Therefore, the HER performance was evaluated based on the anodic scan polarization curve.

Subsequently, potential-controlled EIS measurements were performed at $E = -0.4$ to −0.8 V vs. RHE in 0.05 V intervals. The potential amplitude was 10 mV, the frequency range was 3×10^5 to 1×10^0 Hz, and sampling was repeated several times (60 times when $|E|$ was 0.7–0.8 V vs. RHE; 40 times when $|E|$ was 0.5–0.65 V vs. RHE; and 10 times when $|E|$ was 0.4 V vs. RHE); the average value at each frequency was obtained. The EIS current density changed with frequency during the constant-potential measurements; therefore, the EIS current density at each potential was represented using the current value at the lowest frequency that was closest to the direct-current condition. Following EIS, CV was performed again under the same conditions. The polarization curves before and after EIS showed good agreement (Fig. S3), confirming that the electrochemical properties did not change over time. After a series of electrochemical measurements, the bubble formation behavior during constant-current electrolysis under 14 conditions ($0.1 < -i_{geo} < 2.0$ A cm^{-2}) was recorded using a high-speed video camera (FASTCAM® NOVA S12, Photron Ltd., Japan).

2.3. Pretreatment conditions

Preliminary experiments confirmed that the HER performance deteriorated when energizing a higher (more positive) current density than the Tafel region. It has been reported that hydroxides and hydrogen compounds form on the electrode surface when energizing at potentials above $E = -0.2$ V vs. RHE [25], which may be a factor in the deteriorated HER performance. Therefore, pretreatment was performed over a CV range of −0.3 to −1.0 V vs. RHE. Furthermore, because the HER performance deteriorated during EIS at $E = -0.4$ V vs. RHE, the measurement time under these conditions was shortened to ~3 min by decreasing the sampling number to ten. High-speed video camera observations confirmed that bubbles started to form at a potential of $E = -0.3$ vs. RHE. During CV pretreatment, the HER performance deteriorated during the initial 50 cycles, then improved as the cycle number increased. The change in the polarization curve over time gradually decreased as the number of cycles approached 1000 (Figs. S4 and S5); thus, the optimal pretreatment condition was defined as 1000 cycles.

2.4. In situ observation of hydrogen bubble generation

Fig. 1 shows the system employed for *in situ* bubble generation observations. Constant-current electrolysis was performed at $0.12 < -i_{geo} < 2.0$ A cm^{-2}, and the generation of bubbles from the working electrode was recorded under each condition using a high-speed video camera (1024 × 1024 pixels) at an optical magnification of 20 ×, frame rate of 6000 fps, and shutter speed of 1/6000 s. Halogen light (375 W) was irradiated from both sides of the lens [5,6].

3. Results and discussion

3.1. Relationship between HER polarization curves and bubble generation

Fig. 2 shows the polarization curves recorded from CV measurements using different electrode diameters. Tafel slopes of 120–130 mV dec^{-1} were recorded for all electrode diameters in the range of $0.1 < -i_{geo} < 0.3$ A cm^{-2}, as indicated by the orange shading in Fig. 2. The range of the Tafel region and the slope values were calculated from the plot of dE d
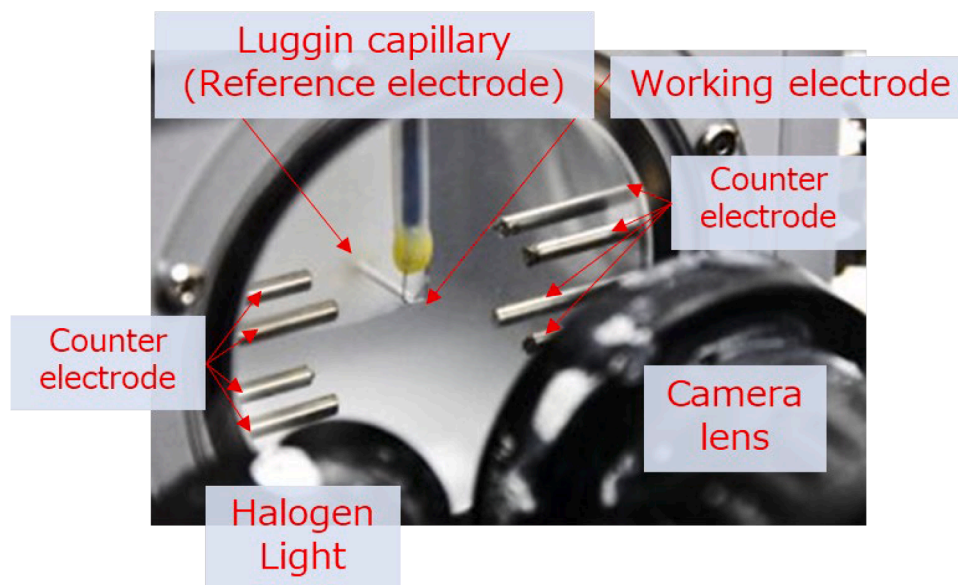
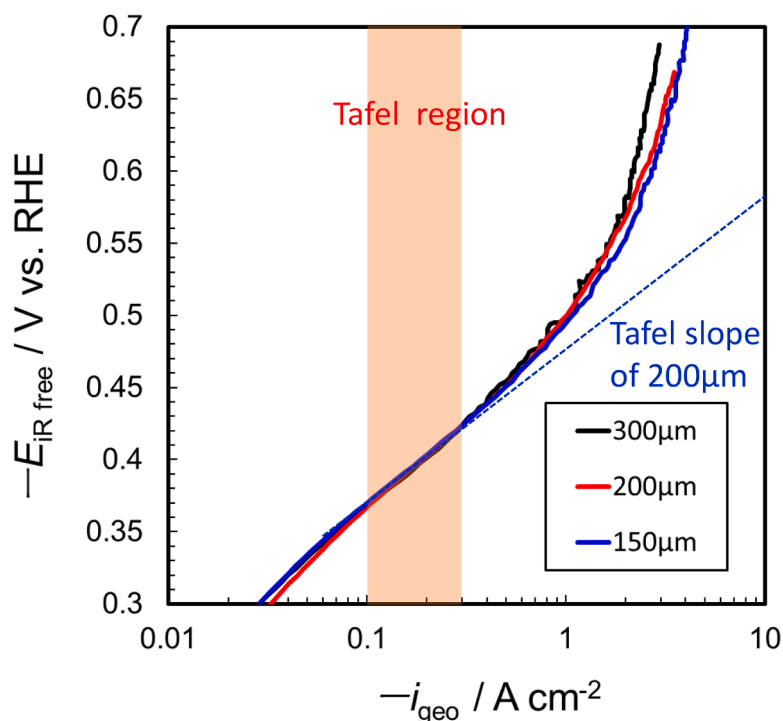**Fig. 1.** *In situ* bubble generation observation system.

Fig. 2. Polarization curves recorded for Ni wire cathodes of different diameters.

$(\log(i_{geo}))^{-1}$ vs. i_{geo} (Fig. S6). The obtained values were in good agreement with those reported in several previous studies on the HER [22,23, 26–29]. Notably, for the $-i_{geo} > 0.3$ A cm^{-2} condition, the polarization curve deviated from the Tafel slope, with a larger electrode diameter leading to a greater degree of deviation above $-i_{geo} \approx 1.0$ A cm^{-2}.

Movie 1 shows a slow-motion movie of bubble formation on a 200 µm Ni electrode at i_{geo} values of (a) −0.1, (b) −0.4, (c) −1.0, and (d) −2.0 A cm^{-2}. Fig. 3 shows snapshots from Movie 1. In addition, Fig. 4 shows the Cole–Cole plots recorded for the 200 µm working electrode at $-i_{geo}$ values of (a) 0.16 A cm^{-2}, and (b) 0.43, 1.00, and 2.04 A cm^{-2}. At $-i_{geo} = 0.16$ A cm^{-2}, although some bubble formation occurred (Fig. 3 (a)), the bubbles had little effect on the electrochemical reaction (Fig. 4

(a)); therefore, the obtained results were used to calculate the solution resistance in the bulk, R_{s0}. It was found that, in the range up to $-i_{geo} <$ 0.4 A cm^{-2}, where only a slight decrease in electrolysis efficiency was observed (Figs. 2 and S6), the number of bubble generation sites increased with increasing $|i_{geo}|$, and the size of the bubbles on the electrode became homogenous (Figs. 3(a) and 3(b)). Notably, the isolated large bubbles that were observed on the electrode surface at $-i_{geo}$ = 0.16 A cm^{-2} disappeared by $-i_{geo} = 0.4$ A cm^{-2}. In addition, Figs. 3(c) and 3(d) show that fine bubbles densely covered the entire electrode surface at high current densities, with increasing values of $|i_{geo}|$ leading to larger bubbles and a more pronounced HER performance reduction. On the other hand, it can be seen from Fig. 4(b) that at $-i_{geo} > 0.4$ A
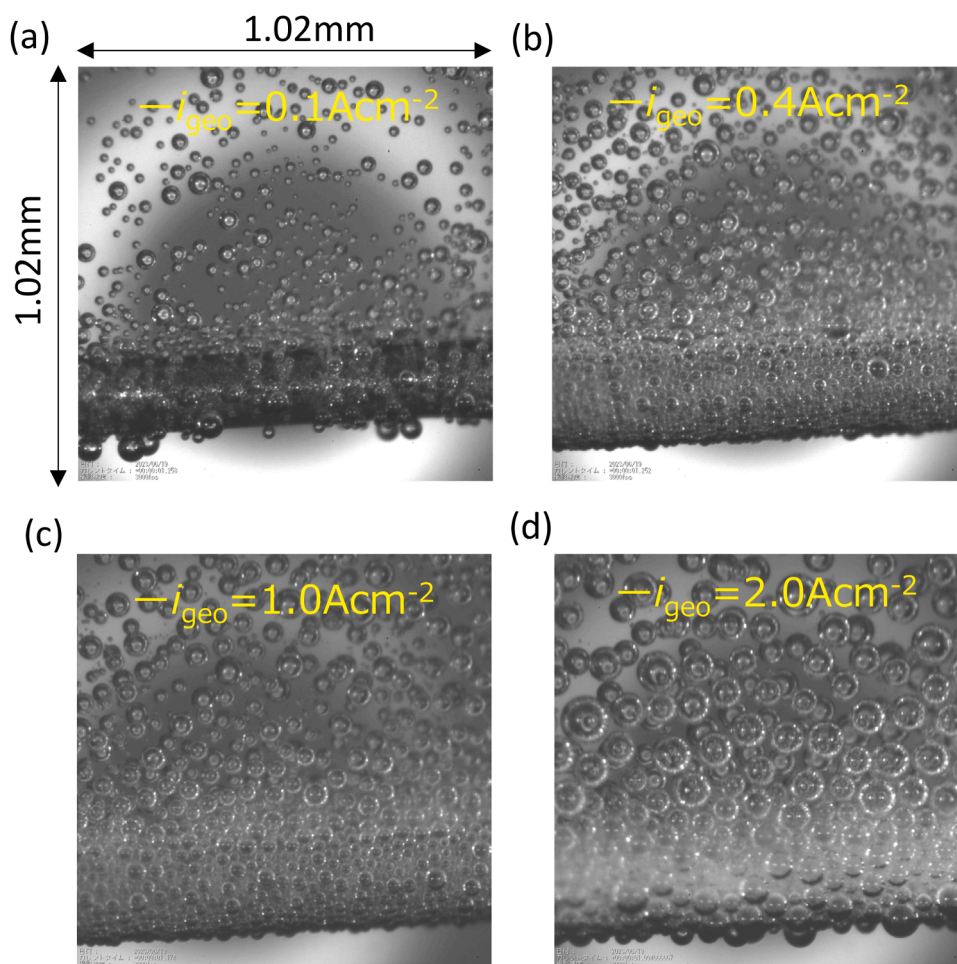
Fig. 3. Photographic images of hydrogen bubble generation under steady state conditions using a 200 μm Ni wire cathode: (a) $-i_{geo}$ = 0.1 A cm^{-2}, (b) $-i_{geo}$ = 0.4 A cm^{-2}, (c) $-i_{geo}$ = 1.0 A cm^{-2}, and (d) $-i_{geo}$ = 2.0 A cm^{-2}.
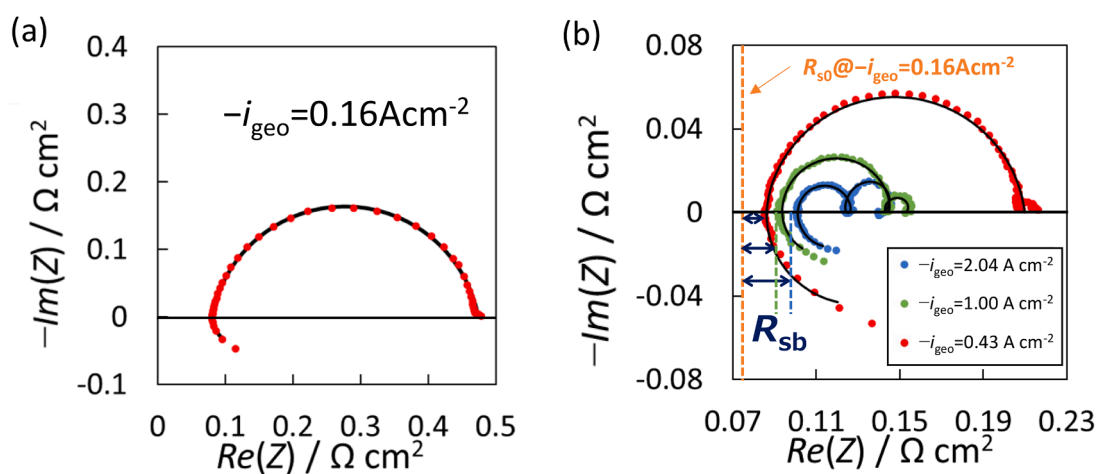

Fig. 4. Cole–Cole plots recorded for the 200 μm Ni wire cathode at different current densities: (a) $-i_{geo}$ = 0.16 A cm^{-2}, and (b) $-i_{geo}$ = 0.43 A cm^{-2}, $-i_{geo}$ = 1.0 A cm^{-2}, and $-i_{geo}$ = 2.0 A cm^{-2}. The solid lines show the results of fitting using the equivalent circuit model in Fig. 6.

cm^{-2}, a new resistance component appeared at low frequencies, in addition to the charge-transfer resistance. This resistance component increased with increasing $|i_{geo}|$. The resistance R_{sb}, which was evaluated using the intersection between the Cole–Cole plot and the real axis on the high-frequency side, also increased with $|i_{geo}|$. These results suggest that the presence of a bubble layer covering the electrode surface increases the solution resistance and induces a new capacitive reactance.

3.2. Equivalent circuit models for the HER at a high current density, and relationship between the charge-transfer resistance and current density

Figure 5(a) illustrates the relationship between the Cole–Cole plots at

$-i_{geo} = 2.04$ A cm^{-2} and each resistance component obtained by equivalent circuits analysis, while Fig. 5(b) shows the Bode impedance diagram plotted at the same current density. In addition, Fig. 6 shows the equivalent circuits at a high current density, wherein the capacitive reactance appears on the low-frequency side. In Fig. 5, the capacitive semicircle corresponding to the electrical double layer is slightly flattened ($10^3 < f < 10^5$ Hz), and so it was modeled using constant phase elements (CPEs, Q_{dl}) instead of a capacitor. An inductive semicircle (R_{L2}) appears on the low-frequency side ($10^2 < f < 10^3$ Hz) of the CPE, while a capacitive semicircle (R_{bub}) and inductive semicircle (R_{L3}) appear at even lower frequencies ($f < 10^2$ Hz). In addition, as shown in Fig. 4(b), the solution resistance, indicated by the intersection between the Cole–Cole plot and the real axis on the high-frequency side, increases with $|i_{geo}|$ because of the bubble coverage layer. The solution resistance at $E = -0.4$ V vs. RHE ($-i_{geo} = 0.16$ A cm^{-2}), where the effect of the bubbles is negligible, is defined as R_{s0}, while the increase in the solution resistance with reference to R_{s0} is defined as R_{sb}. According to the dual-bubble layer model [5] proposed for the anode reaction, R_{sb} corresponds to the additional ohmic resistance caused by the bubble coverage layer on the electrode. However, the equivalent circuit modeled using a resistor–capacitor circuit without a coil on the low-frequency side ($1 < f < 10^2$ Hz; Fig. S7(a)) and an equivalent circuit modeled with a Warburg

impedance on the low-frequency side (Fig. S7(b)) did not accurately fit the Cole–Cole plots (Fig. S8).

As shown in Eq. (6), the derivative of the potential with regard to the current density in the polarization curve is equal to the sum of the resistance components that are obtained by Cole–Cole plot equivalent circuit analysis, namely, the solution resistance in the bulk, R_{s0}; the increase in solution resistance in the bubble coverage layer, R_{sb}; the apparent charge-transfer resistance, R_{p1}, due to charge-transfer resistance R_{ct} (CPE) and R_{L2}; and the apparent diffusion resistance in the bubble coverage layer, R_{p2}, due to R_{bub} and R_{L3}.

$$\frac{dE}{di_{geo}} = R_{s0} + R_{sb} + R_{p1} + R_{p2} \qquad (6)$$

In Section 3.3, models of the phenomena associated with each resistance component are presented, wherein R_{s0} corresponds to the solution resistance in the bubble-free solution and R_{sb} originates from obstructed charge carrier (OH$^-$) migration by the bubble coverage layer formed on the electrode surface. R_{sb} can be explained by considering the decrease in the apparent electrical conductivity based on the tortuosity degree. The R_{sb} value of the cathode is discussed in detail in Section 3.5. In addition, R_{p1} is the apparent charge-transfer resistance calculated by subtracting the negative resistance R_{L2} (modeled by the inductive
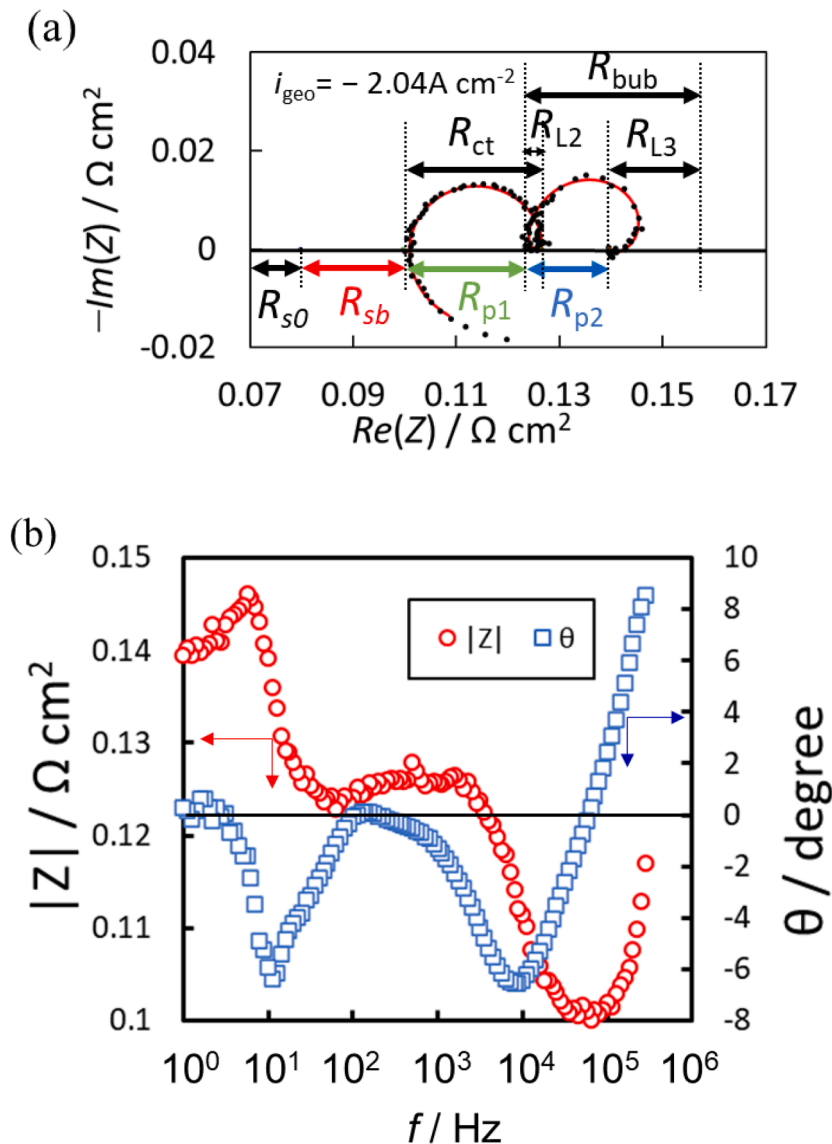

Fig. 5. (a) Cole–Cole plots and the different resistance components. (b) Bode impedance diagram ($-i_{geo} = 2.04$ A cm^{-2}).

semicircle associated with H_{OPD} adsorption) from R_{ct}. In Section 3.3, the relationship between the CPE, R_{L2}, and bubble generation at each current density is discussed. It should be noted here that R_{p2} is the apparent diffusion resistance induced at low frequencies ($f < 10^2$ Hz), and is calculated by subtracting the negative resistance R_{L3} (modeled by an inductive semicircle at the low-frequency side and associated with enhanced bubble detachment) from the diffusion resistance R_{bub} (modeled by a capacitive semicircle). R_{p2} is discussed in detail in Section 3.4. Finally, Section 3.6 provides a comparison to the anode phenomenological model proposed by our research group.

Fig. 7 shows the logarithmic plot of R_{ct} for the 200 μm working electrode, wherein it can be seen that even at a high current density ($-i_{geo} > 0.3$ A cm^{-2}), where the polarization curve deviates from the Tafel slope, R_{ct} is inversely proportional to i_{geo}. The relationship between R_{ct} and i_{geo} can therefore be expressed as

$$R_{ct} = 0.054\, i_{geo}^{-1} \tag{7}$$

Thus, the Tafel slope can be expressed as

$$\ln 10\ \times\ 0.054 = 0.124\ \text{V dec}^{-1} \tag{8}$$

This value is very close to the Tafel slope obtained from the CV measurements, thereby indicating that even at high current densities ($-i_{geo} > 0.3$ A cm^{-2}) where the electrode surface is covered by bubbles and the HER efficiency is reduced, the electrode surface is sufficiently wet, and no reduction in the effective reaction area is observed for electrolytic reactions caused by drying of the electrode surface.

3.3. Modeling of H_{OPD} and bubble generation on the electrode surfaces

As discussed above, the HER occurs in two steps, namely the Volmer reaction (Eq. (1)) and the Heyrovsky reaction (Eq. (2)), where the reaction intermediate, a hydrogen atom (H_{OPD}), is adsorbed onto the metal electrode surface [19–21]. In general, the inductive semicircle formed on the low-frequency side of the capacitive semicircle corresponding to R_{ct} in a Cole–Cole plot corresponds to the negative resistance that forms as the adsorption of reaction-enhancing adsorbents (e.g., reaction intermediates) increases at higher current densities [21,30]. Here, this inductive semicircle is considered to correspond to the increased adsorption of H_{OPD} as the potential becomes more negative; this is quantified as R_{L2} based on the inductive semicircle formed at $10^2 < f < 10^3$ Hz (see Fig. 5). In contrast, the capacitive semicircle in the high frequency region, which corresponds to the electrical double layer, flattens slightly at $0.16 < -i_{geo} < 1.5$ A cm^{-2}. In addition, the degree of flattening decreases with increasing current density, resulting in a perfect arc at $-i_{geo} > 1.5$ A cm^{-2}. Previously, it has been reported that at $-i_{geo} < 0.16$ A cm^{-2}, a flatter capacitive semicircle appears [22,23], and this phenomenon can be modeled by a CPE, as shown in the equivalent circuit presented in Fig. 6. This is possible due to the non-homogeneous adsorption of chemical species on the electrode surface [31,32], which, in the HER, is thought to arise from the non-homogeneous adsorption of reaction intermediates (H_{OPD}). From these analyses, it appears that the amount of H_{OPD} adsorbed on the electrode surface increases with increasing current density, and at high current densities, H_{OPD}
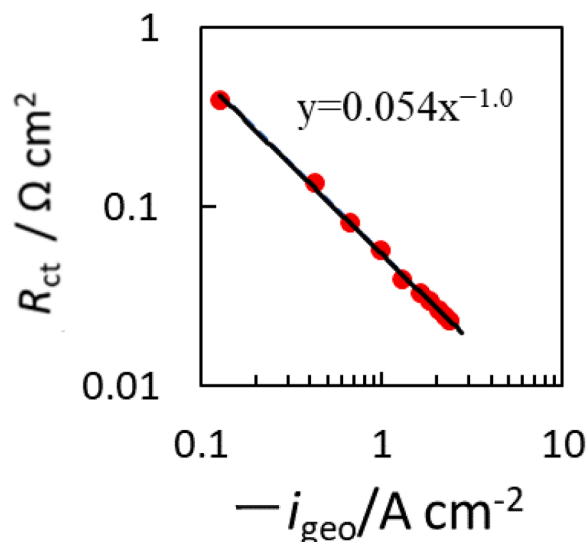

Fig. 7. Relationship between current density $-i_{geo}$ and charge-transfer resistance R_{ct} for a 200 μm Ni working electrode.

homogeneously cover the entire surface of the electrode. These results were also confirmed for electrodes of different diameters (Figs. S10–S12).

Fig. 8 shows schematics of the electrode surfaces devised in this study for (a) the Tafel region ($0.1 < -i_{geo} < 0.3$ A cm^{-2}), (b) the upper limit of the Tafel region ($0.3 < -i_{geo} < 0.4$ A cm^{-2}), (c) the bubble coverage region ($-i_{geo} = 1.0$ A cm^{-2}), and (d) the bubble coalescence region ($-i_{geo} = 2.0$ A cm^{-2}). Figs. 3(a) and 3(b) and Figs. 8(a) and 8(b) show that, in the Tafel region, the number of bubbles generated increases with increasing current density, resulting in smaller and more homogeneous bubbles that densely cover the electrode surface. This was attributed to an increase in the bubble generation area due to an increase in the amount of adsorbed H_{OPD} at higher current densities. In addition, at high current densities (Figs. 3(c) and 3(d) and Figs. 8(c) and 8(d)), bubbles densely cover the electrode surface and bubble coalescence increases. As a result, the bubble diameter increases, and the bubble coverage layer becomes thicker. This dense bubble layer inhibits the migration and diffusion of substances from the electrode surface.

Based on these findings, the relationship between the rate-limiting reaction of the HER and the Tafel slope was investigated. It has been generally accepted that the rate-limiting steps for Tafel slopes of 120 and 40 mV dec^{-1} are the Volmer and Heyrovsky reactions, respectively [19, 20]. However, in their simulations on the effect of the H_{OPD} adsorption rate, Shinagawa et al. [20] reported that when the Tafel slope is equal to 120 mV dec^{-1}, the Heyrovsky reaction can be the rate-limiting step when the H_{OPD} coverage is >0.6, while the Volmer reaction can be the rate-limiting step when the H_{OPD} coverage is close to zero [20,21]. Thus, the H_{OPD} coverage appears to play a significant role in determining the rate-limiting step of the HER. In the current study, the obtained Cole–Cole plots suggest that H_{OPD} adsorption increases with increasing
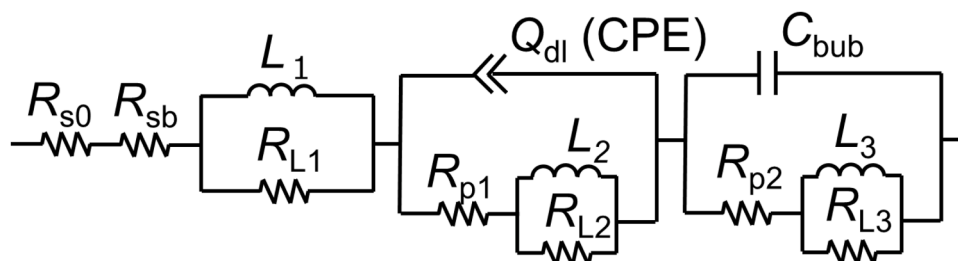

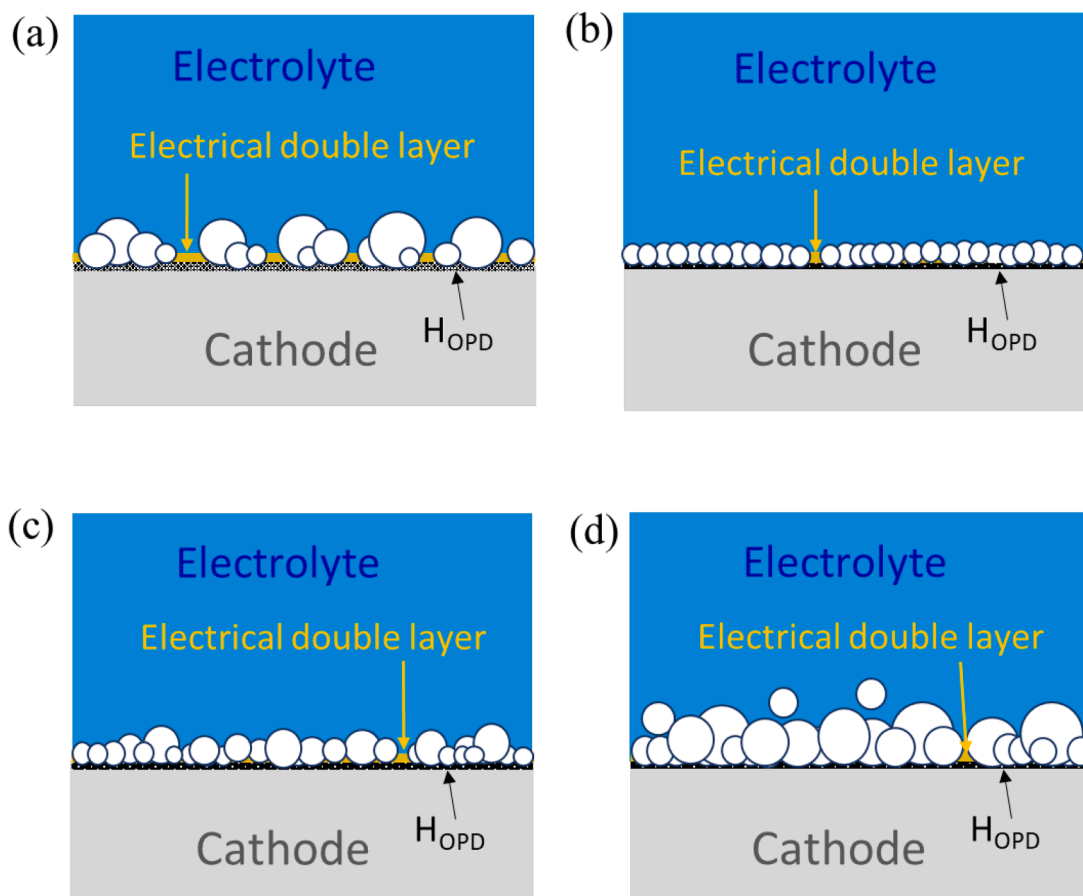**Fig. 6.** Equivalent circuit of the HER at a high current density.

Fig. 8. Schematics of the electrode surface at (a) $-i_{geo} = 0.1$ A cm^{-2} (Tafel region), (b) $-i_{geo} = 0.4$ A cm^{-2}, (c) $-i_{geo} = 1.0$ A cm^{-2}, and (d) $-i_{geo} = 2.0$ A cm^{-2}.

current density until covering the electrode surface and giving a Tafel slope of 120 mV dec^{-1}; in this case, the rate-limiting step was defined as the Heyrovsky reaction. Notably, these results are consistent with those reported by Shinagawa et al. [20]. Moreover, Jantz et al. [16] also concluded that the Heyrovsky reaction is the rate-limiting step in experiments with similar H$_{OPD}$ adsorption rates and Tafel slopes.

3.4. Diffusion resistance (R_{p2}) on the low-frequency side

In the high-current-density region, where the polarization curve deviated from the Tafel slope and the HER performance decreased, the electrode surface was densely covered with small bubbles (see Figs. 3(c) and 3(d)). Upon increasing the current density, the bubbles coalesced, the bubble diameters increased, and the bubble coverage layer thickened. In the Cole–Cole plots, capacitive and inductive semicircles appeared on the low-frequency side (see Fig. 4), suggesting that the bubble layer was so dense that bubble coalescence inhibited ion migration and substance diffusion from the electrode surface. Previously, our group reported that, for the anodic reaction of AWE, the increased ohmic resistance caused by the bubble coverage layer on the electrode surface can be modeled based on the layer thickness and tortuosity degree. In addition, the diffusion resistance of the reactant OH$^-$ could be modeled by Warburg impedance [5]. Therefore, we modeled the ohmic and diffusion resistances in the presence of a bubble coverage layer for the cathodic reaction. The resistance corresponding to the capacitive semicircle on the low-frequency side of the Cole–Cole plots (i. e., <100 Hz, Fig. 5) was defined as the diffusion resistance caused by bubble coverage, R_{bub}, whereas the resistance corresponding to the inductive semicircle was defined as the negative resistance, R_{L3}, which is related to the promotion of bubble release. The resistance corresponding

to the difference between R_{bub} and R_{L3} was defined as the apparent diffusion resistance, R_{p2}.

Fig. 9 shows the relationship between R_{p2} and the current density for each electrode diameter examined herein, while the relationship between R_{bub} and R_{L3}, which constitute R_{p2}, and the current density is shown in Fig. S13. From Fig. 9, it can be seen that R_{p2} increased gradually with increasing current density and electrode diameter. Similar behavior was measured for the diffusion resistance R_d of OH$^-$ in the
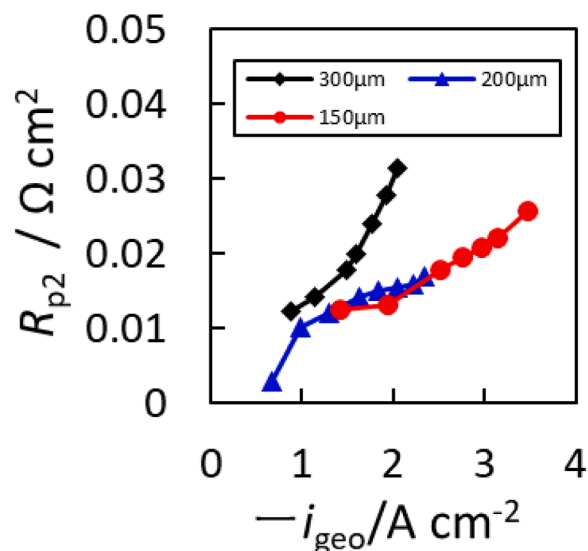

Fig. 9. Variation in R_{p2} with $-i_{geo}$ for the three electrode diameters.

anodic reaction [5]; that is, the resistance increased with increasing current density and electrode diameter. As shown in Fig. 5 and Movie 1 (played at $1/100\times$ speed), bubble generation occurs at ~100 Hz, while R_{p2} appears at a lower frequency range lower than this bubble generation frequency (i.e., $f < 10^2$ Hz). These results indicate that R_{p2} and its components R_{bub} and R_{L3} are expected to be caused by bubble generation.

Subsequently, the origin of R_{bub}, induced by bubble coverage, was considered. In the anodic reaction of AWE, a concentration gradient of OH^- is formed close to the electrode because the numerous bubbles generated on the electrode surface inhibit the supply of the reactant OH^- to the electrode surface [5]. In the Cole–Cole plots, Warburg impedance with finite diffusion appeared at the lower frequency side (<100 Hz), which can be quantified as the diffusion resistance R_d (Ω cm^2). In contrast, at the cathode, OH^- is produced via an electrochemical reaction and transported via convective diffusion from the electrode surface toward the solution bulk as the bubbles leave the cathode. Therefore, OH^- diffusion is not restricted at the cathode. In addition, in the 2 M KOH electrolyte, the cathode reactant (H_2O) is more abundant in solution than the anodic reactant (OH^-) (concentrations of H_2O is 55.5 and OH^- is 2 mol L^{-1}, respectively). Therefore, H_2O is unlikely to be a diffusion rate-limiting substance. However, it is conceivable that the pH in the vicinity of the electrode may be increased due to the simultaneous increase/decrease in OH^-/H_2O in the cathodic reaction. Therefore, the pH near the electrode and the pH near the RHE may have been misaligned, resulting in an apparent performance deterioration. In another study, two capacitive semicircles originating from the electrolytic reaction were observed at $0.05 < |E| < 0.2$ V vs. RHE [22, 23]; however, these resistances were inversely proportional to the current density, whereas R_{bub} increases with current density. Thus, they are considered to be different resistance factors.

R_{L3} is the negative resistance associated with reaction promotion. It corresponds to the inductive semicircle in the Cole–Cole plots. Notably, adsorbates that appear as inductive semicircles generally either promote electrochemical reactions (wherein the amount of adsorption increases with increasing current density) or prevent reactions (wherein the amount of adsorption decreases with increasing current density). The discussions presented in Supplementary Text S2 [21,30,33] suggest that, because the bubbles produced in alkaline solutions are reported to possess negative zeta potentials [34], R_{L3} could be considered a negative resistance component associated with enhanced detachment of reaction-preventing adsorbed bubbles from the negatively charged cathode surface as the cathode potential becomes more negative.

3.5. Ohmic resistance originating from the bubble coverage layer

As mentioned above, based on the Tafel region, the solution resistance at $E = -0.4$ V vs. RHE ($-i_{geo} = 0.16$ A cm^{-2}), where few bubbles were formed, was defined as R_{s0}. In addition, the increase in solution resistance in the bubble coverage layer at increasing current densities with reference to R_{s0} was defined as R_{sb}. Furthermore, $R_{s0} + R_{sb}$ corresponds to the high-frequency intercept of the Cole–Cole plot. Thus, Fig. 10 shows the relationship between R_{sb} and the current density for each electrode diameter, wherein it can be seen that R_{sb} increases gradually with increasing current density and electrode diameter. This increase in the solution resistance can be attributed to the fact that the charged OH^- ions migrate a long distance from the electrode surface to the bulk solution through the gaps between bubbles in the bubble coverage layer. Moreover, Fig. 11 shows the relationship between the bubble coverage layer thickness (δ_b, cm, calculated from the photographic images in Fig. S14) and the current density for each electrode diameter. In this case, it is clear that δ_b increases gradually with the current density and becomes thicker for larger electrode diameters. Thus, as in the case of the anodic reaction [5], the behavior of R_{sb} was modeled for the cathodic reaction based on δ_b and the degree of tortuosity.
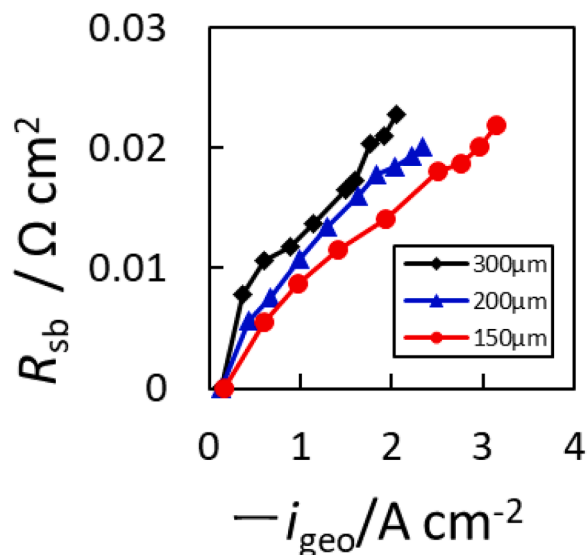

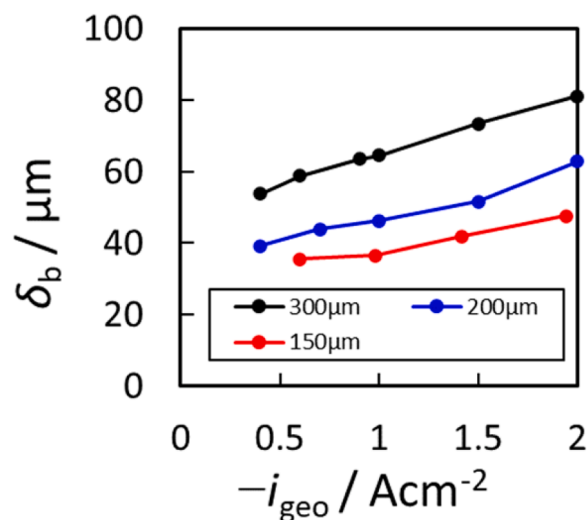**Fig. 10.** Relationship between R_{sb} and $-i_{geo}$ for each electrode diameter.

Fig. 11. Relationship between δ_b and $-i_{geo}$ for each electrode diameter.

The ohmic resistance in a layer of solution, having the same thickness as the bubble coverage layer, can be expressed as $\delta_b(S_{bubble})^{-1}\kappa^{-1}S_{geo}$, where κ (S m^{-1}) is the electrical conductivity of the electrolyte solution (2 M KOH at 30 °C) and S_{bubble} (cm^2) is the average of the geometric surface area of the electrode ($S_{geo} = \pi D L_{WE}$) and the area outside the bubble coverage layer ($2\pi L_{WE}(\delta_b + D/2)$), as calculated using Eq. (9):

$$S_{bubble} = \frac{2\pi L_{WE}\delta_b}{\ln\left(\frac{\delta_b + D/2}{D/2}\right)}. \tag{9}$$

On the other hand, the ohmic resistance in the bubble coverage layer can be expressed as $\delta_b(S_{bubble})^{-1}\kappa^{-1}(1-\varepsilon)^{-x}S_{geo}$ (Ω cm^2), where $(1-\varepsilon)^{-x}$ is the tortuosity degree, ε is the void fraction of the bubble coverage layer, and x is a constant in the Bruggeman equation [35]. Therefore, the relationship between R_{sb} (quantified from the EIS measurements) and the tortuosity degree of the bubble coverage layer can be derived using Eq. (10).

$$R_{sb} = \delta_b(S_{bubble})^{-1}\kappa^{-1}(1-\varepsilon)^{-x}S_{geo} - \delta_b(S_{bubble})^{-1}\kappa^{-1}S_{geo}, \tag{10}$$

where the equations defined for the anode reaction [5] are applied to the

cathode. In Eq. (10), the value of x in $(1 - \varepsilon)^{-x}$ is assumed to be constant [36] irrespective of the current density, similarly to that of the anode. A value of 1.43 was selected for x, since no significant differences were observed over the range of $x = 1.41$–1.46.

In a previous report [5], the ε value of the anode was treated as a constant with respect to the current density, but in practice, ε is expected to change with the current density. Thus, a model in which ε changes with current density was investigated. Using $x = 1.43$, ε was evaluated for each current density using Eq. (10), and the results are presented in Fig. 12. ε increases gradually from 0.35 to 0.51 upon increasing the current density. At high current densities, the value is close to the close-packed structure of uniformly sized spheres ($\varepsilon \approx 0.6$). In addition, the slight variation in the void fraction and tortuosity degree for the three electrode diameters indicates that the difference in R_{sb} with electrode diameter shown in Fig. 10 is mainly caused by the varying bubble coverage layer thicknesses, δ_b, associated with these electrodes (see Fig. 11).

3.6. Comparison of resistance components between the cathode and anode

The effects of the bubbles on the anodic and cathodic reactions were subsequently compared, as presented in Figs. 13–15 for the bubble generation behavior (at $|i_{geo}| = 1.0$ A cm^{-2}), δ_b, and R_{sb}, respectively. Schematic definition of δ_b is shown in Fig. S14. As shown in Figs. 13 and 14, the hydrogen bubbles at the cathode are significantly smaller than the oxygen bubbles at the anode, and the bubble coverage layer is thinner at the cathode than the anode. In addition, the results presented in Fig. 15 show that R_{sb} is smaller for the cathode. As presented in Table 1 and Fig. S15, although there is a large difference in the bubble diameters between the anode and the cathode, the differences in $(1 - \varepsilon)^{-x}$ and ε are small, with tortuosity degrees of 2.40 and 2.11 being determined for the anode and the cathode, respectively. As a result, the value of R_{sb} is smaller for the cathode, which possesses a smaller δ_b value.

Fig. 16 shows the diffusion resistance R_d in the bubble coverage layer for the OER at a high current density and the apparent diffusion resistance R_{p2}, corresponding to the difference between R_{bub} and R_{L3}, in the bubble coverage layer for the HER. Both diffusion resistances appear on the low-frequency side of the Cole–Cole plots at high current densities, and the diffusion resistances were significantly higher for the OER regardless of electrode size.

Finally, Fig. 17 shows the anodic and cathodic polarization curves recorded using the 200 μm electrode. For this purpose, the overvoltage $\Delta \eta$ (V) of the anode and cathode was defined as the difference between the $E_{iR\ free}$ (V vs. RHE) values obtained from the CV measurements and the theoretical decomposition voltage (0 V vs. RHE for the cathode and 1.23 V vs. RHE for the anode). As a result, Tafel slopes of ~127 and 49 mV dec^{-1} were determined for the HER and OER, respectively. Based on comparisons of the Tafel slopes, the performance of the HER was worse than that of the OER. However, in the high-current-density region where the polarization curve deviates from the Tafel slope, the overvoltage of the OER is similar to that of the HER at $|i_{geo}| \approx 2.0$ A cm^{-2}, because the effect of $R_{sb} + R_d$ is larger for the OER in the presence of a bubble layer.

4. Conclusion

A method was proposed for separating and quantifying the resistance components caused by bubbles, which is responsible for the overvoltage increase during the cathodic hydrogen evolution reaction (HER) of alkaline water electrolysis (AWE) using a Ni wire electrode. The method employed a high-speed video camera, cyclic voltammetry (CV), electrochemical impedance spectroscopy (EIS), and equivalent circuit analysis. CV measurements showed that, at current densities ($-i_{geo}$) of > 0.3 A cm^{-2}, the polarization curve deviated from the Tafel slope due to bubble coverage, resulting in reduced performance. The Cole–Cole plots obtained from the EIS measurements consisted of two pairs of capacitive and inductive semicircles. The equivalent circuit model was devised to separate and quantify the resistance at each current density.

The resistance components included the apparent charge-transfer resistance R_{p1}, which is composed of the charge-transfer resistance R_{ct} and a negative resistance R_{L2}, modeled by the inductive semicircle associated with the adsorption of HER intermediates H_{OPD} (hydrogen atoms, OPD = overpotential deposition). R_{ct} was found to be inversely proportional to the current density even at high current densities. This means that the effective electrode surface area remained unchanged even when the electrode surface was completely covered with bubbles. R_{L2} may arise because the H_{OPD} content increases as the potential becomes more negative, thereby promoting the reaction. On the other hand, the increase in solution resistance within the bubble coverage layer, R_{sb}, is attributed to the fact that the OH$^-$ charge carriers migrate long distances from the electrode surface toward the bulk solution through the gaps between bubbles. R_{sb} is quantified as a product of the bubble coverage layer thickness, δ_b, and the decrease in electrical conductivity modeled by the degree of tortuosity, $(1 - \varepsilon)^{-x}$. Another pair of capacitive and inductive semicircles were observed in the low-frequency region ($1 < f < 100$ Hz) in the Cole–Cole plots, which correspond to the frequency of bubble generation, as observed by the high-speed video camera. These semicircles were modeled by the apparent diffusion resistance R_{p2}, which comprised the diffusion resistance induced by the bubble coverage layer, R_{bub}, quantified by the capacitive semicircle, and a negative resistance R_{L3}, modeled by the inductive semicircle. R_{L3} is
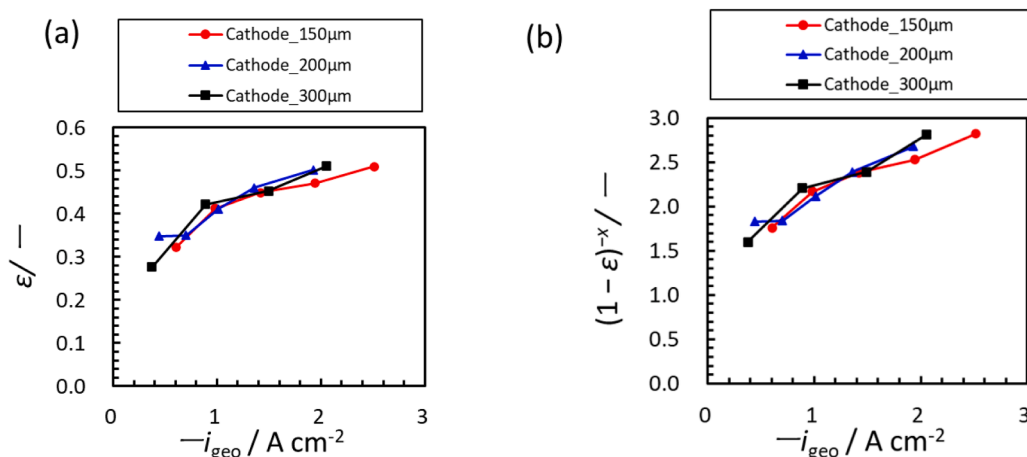

Fig. 12. Relationship between $-i_{geo}$ and (a) void fraction of the bubble coverage layer ε and (b) degree of tortuosity $(1 - \varepsilon)^{-x}$.
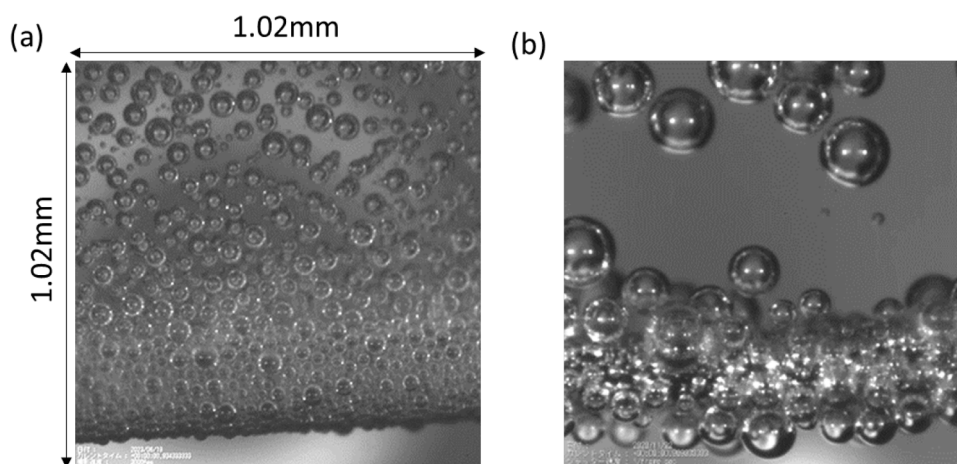
Fig. 13. Photographic images of bubble coverage layers on (a) the cathode and (b) the anode (200 μm Ni wire electrode, $|i_{geo}| = 1.0$ A cm^{-2}).

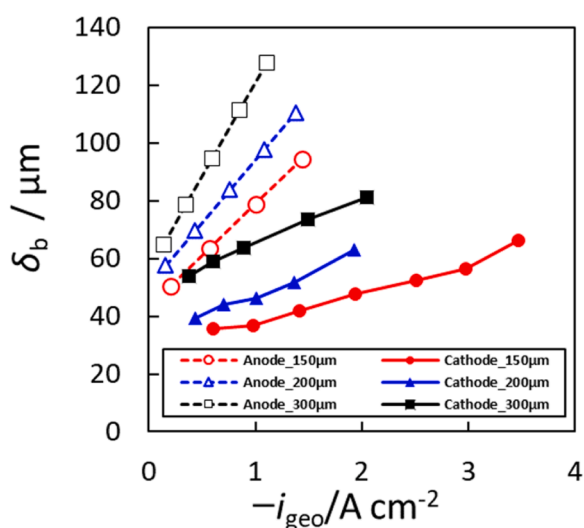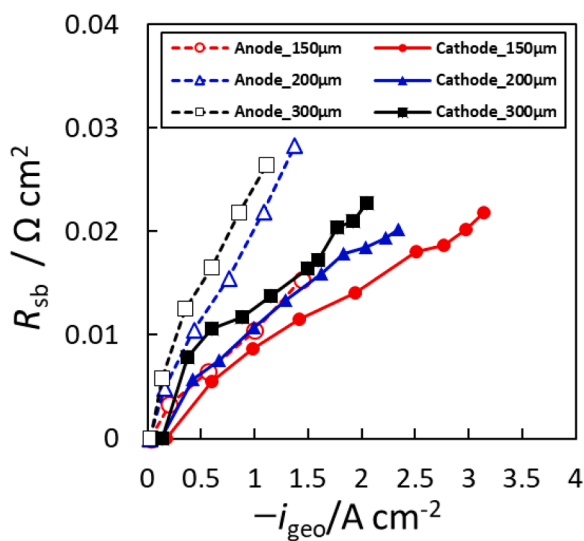**Fig. 14.** Bubble layer thickness δ_b for various cathodes and anodes.

Fig. 15. Comparison of R_{sb} for various cathodes and anodes.

Table 1
Bubble layer properties at the anode and cathode ($|i_{geo}| = 1.0$ A cm^{-2}).

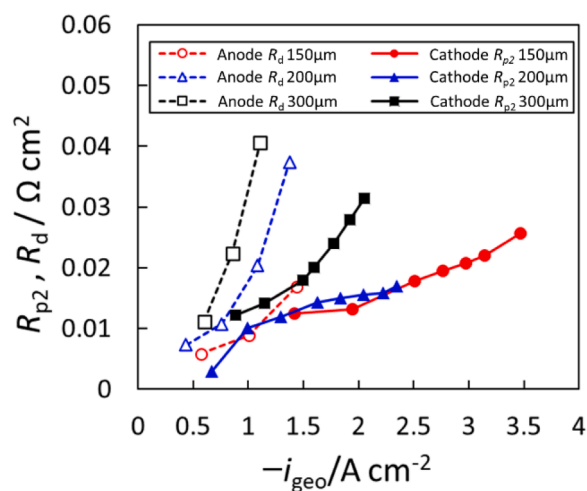|	Tortuosity degree $(1 - \varepsilon)^{-x}$	Void fraction ε / –	Constant of the Bruggeman equation x / –	δ_b / μm	R_{sb} / Ω cm^2
Cathode	2.11	0.41	1.43	46.2	0.011
Anode	2.40	0.46	1.43	97.6	0.022

Fig. 16. Comparison between apparent diffusion resistance R_{p2} in the bubble coverage layer at the cathode and diffusion resistance R_d in the bubble coverage layer at the anode.

thought to be induced by the enhanced release of negatively charged bubbles from the electrode as the potential becomes more negative. From the above, it was found that the increase in overvoltage at high current densities during the HER was not due to a reduction in the effective electrode area for the reaction but was instead caused by the ohmic resistance R_{sb} and apparent diffusion resistance R_{p2} caused by the dense bubble coverage on the electrode surface.

The obtained results were compared with those of previous studies into the resistance components of the OER using Ni wire electrodes. It was found that R_{sb} and R_{p2} caused by bubbles on the cathode surface were both smaller than the corresponding values (R_{sb} and R_d) for the anode. Although the apparent electrical conductivity of the bubble coverage layer modeled by the tortuosity degree was not found to be significantly different between the anode and cathode, the larger
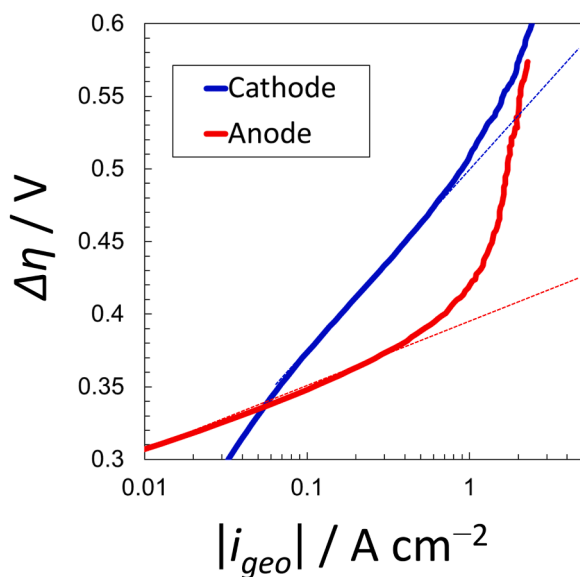
Fig. 17. Comparison of anodic and cathodic polarization curves (200 μm electrode).

bubbles produced at the anode led to a higher bubble coverage layer thickness δ_b, which in turn led to a larger ohmic resistance R_{sb}. Additionally, the apparent diffusion resistance R_{p2} of the cathode was affected by the negative resistance, unlike that of the anode modeled using the Warburg impedance. The current study also demonstrated that a smaller electrode diameter led to reduced bubble coverage layer thickness and a lesser decline in the HER performance per electrode unit area. However, when designing electrolytic cells, it is necessary to improve the current density per membrane area; this requires the use of densely arranged thin electrodes to increase the total electrode area. Thus, future work should focus on quantifying the effects of bubbles in the presence of such a dense electrode arrangement.

CRediT authorship contribution statement

Daisuke Kitajima: Writing – original draft, Visualization, Methodology, Investigation, Formal analysis, Data curation. **Ryuta Misumi:** Writing – review & editing, Writing – original draft, Validation, Supervision, Project administration, Methodology, Investigation, Conceptualization. **Yoshiyuki Kuroda:** Writing – review & editing, Validation, Resources, Methodology, Investigation. **Shigenori Mitsushima:** Writing – review & editing, Validation, Supervision, Resources, Methodology, Investigation, Funding acquisition.

Declaration of competing interest

The authors declare that they have no known competing financial interests or personal relationships that could have appeared to influence the work reported in this paper.

Data availability

Data will be made available on request.

Acknowledgments

Supplementary materials

Supplementary material associated with this article can be found, in the online version, at doi:10.1016/j.electacta.2024.144772.

References

[1] Th. Boruciński, S. Rausch, H. Wendt, Raney nickel activated H₂-cathodes Part II: correlation of morphology and effective catalytic activity of Raney-nickel coated cathodes, J. Appl. Electrochem. 22 (1992) 1031–1992, https://doi.org/10.1007/bf01029581.

[2] L. Schlapbach, Hydrogen-fuelled vehicles, Nature 460 (2009) 809–811, https://doi.org/10.1038/460809a.

[3] N. Nagai, M. Takeuchi, T. Kimura, T. Oka, Existence of optimum space between electrodes on hydrogen production by water electrolysis, Int. J. Hydrog. Energy 28 (2003) 35–41, https://doi.org/10.1016/S0360-3199(02)00027-7.

[4] M.M. Bakker, D.A. Vermaas, Gas bubble removal in alkaline water electrolysis with utilization of pressure swings, Electrochim. Acta 319 (2019) 148–157, https://doi.org/10.1016/j.electacta.2019.06.049.

[5] H. Ikeda, R. Misumi, Y. Nishiki, Y. Kuroda, S. Mitsushima, A dual bubble layer model for reactant transfer resistance in alkaline water electrolysis, Electrochim. Acta 430 (2022) 141053, https://doi.org/10.1016/j.electacta.2022.141053.

[6] H. Ikeda, R. Misumi, Y. Kojima, A.A. Haleem, Y. Kuroda, S. Mitsushima, Microscopic high-speed video observation of oxygen bubble generation behavior and effects of anode electrode shape on OER performance in alkaline water electrolysis, Int. J. Hydrog. Energy 47 (2022) 11116–11127, https://doi.org/10.1016/j.ijhydene.2022.01.166.

[7] K. Ando, Y. Uchimoto, T. Nakajima, Concentration profile of dissolved gas during hydrogen gas evolution: an optical approach, Chem. Commun. 56 (2020) 14483–14486, https://doi.org/10.1039/D0CC05695B.

[8] K. Ando, Y. Uchimoto, T. Nakajima, Probing the dissolved gas concentration on the electrode through laser-assisted bubbles, J. Phys. Chem. C 125 (2021) 20952–20957, https://doi.org/10.1021/acs.jpcc.1c06816.

[9] D. Zhang, K. Zeng, Evaluating the behavior of electrolytic gas bubbles and their effect on the cell voltage in alkaline water electrolysis, Ind. Eng. Chem. Res. 51 (2012) 13825–13832, https://doi.org/10.1021/ie301029e.

[10] Y. Li, G. Yang, S. Yu, Z. Kang, J. Mo, B. Han, D.A. Talley, F.-Y. Zhang, *In-situ* investigation and modeling of electrochemical reactions with simultaneous oxygen and hydrogen microbubble evolutions in water electrolysis, Int. J. Hydrog. Energy 44 (2019) 28283–28293, https://doi.org/10.1016/j.ijhydene.2019.09.044.

[11] K. Zeng, D. Zhang, Recent progress in alkaline water electrolysis for hydrogen production and applications, Prog. Energy Combust. Sci. 36 (2010) 307–326, https://doi.org/10.1016/j.pecs.2009.11.002.

[12] H. Vogt, R.J. Balzer, The bubble coverage of gas-evolving electrodes in stagnant electrolytes, Electrochim. Acta 50 (2005) 2073–2079, https://doi.org/10.1016/j.electacta.2004.09.025.

[13] J.O'M. Bockris, A.K.N. Reddy, Ion transport in solutions. Modern Electrochemistry 1: Ionics, 2nd ed., Springer, Boston, MA, 1998, pp. 361–599, https://doi.org/10.1007/b114546.

[14] H. Ikeda, R. Misumi, Y. Nishiki, Y. Kuroda, S. Mitsushima, *tert*-Butyl-alcohol-induced breakage of the rigid bubble layer that causes overpotential in the oxygen evolution reaction during alkaline water electrolysis, Electrochim. Acta 452 (2023) 142283, https://doi.org/10.1016/j.electacta.2023.142283.

[15] W. Fogaça, H. Ikeda, R. Misumi, Y. Kuroda, S. Mitsushima, Enhancement of oxygen evolution reaction in alkaline water electrolysis by Lorentz forces generated by an external magnetic field, Int. J. Hydrog. Energy 61 (2024) 1274–1281, https://doi.org/10.1016/j.ijhydene.2024.02.199.

[16] D.T. Jantz, T.E. Seuferling, K.C. Leonard, Numerical deconvolution of surface interrogation scanning electrochemical microscopy experiments on platinum during hydrogen evolution, ChemElectroChem 7 (2020) 4842, https://doi.org/10.1002/celc.202001420.

[17] B.E. Conway, L. Bai, Determination of adsorption of OPD H species in the cathodic hydrogen evolution reaction at Pt in relation to electrocatalysis, J. Electroanal. Chem. Interfacial Electrochem. 198 (1986) 149–175, https://doi.org/10.1016/0022-0728(86)90033-1.

[18] L.E. Botello, J.M. Feliu, V. Climent, Activation energy of hydrogen adsorption on Pt (111) in alkaline media: an impedance spectroscopy study at variable temperatures, ACS Appl. Mater. Interfaces 12 (2020) 42911–42917, https://doi.org/10.1021/acsami.0c13158.

[19] J. Wang, F. Xu, H. Jin, Y. Chen, Y. Wang, Non-noble metal-based carbon composites in hydrogen evolution reaction: fundamentals to applications, Adv. Mater. 29 (2017) 1605838, https://doi.org/10.1021/acsami.0c13158.

[20] T. Shinagawa, A.T. Garcia-Esparza, K. Takanabe, Insight on Tafel slopes from a microkinetic analysis of aqueous electrocatalysis for energy conversion, Sci. Rep. 5 (2015) 13801, https://doi.org/10.1038/srep13801.

[21] A. Lasia, Mechanism and kinetics of the hydrogen evolution reaction, Int. J. Hydrog. Energy 44 (2019) 19484–19518, https://doi.org/10.1016/j.ijhydene.2019.05.183.

[22] C. González-Buch, I. Herraiz-Cardona, E. Ortega, J. García-Antón, V. Pérez-Herranz, Study of the catalytic activity of 3D macroporous Ni and NiMo cathodes for hydrogen production by alkaline water electrolysis, J. Appl. Electrochem. 46 (2016) 791–803, https://doi.org/10.1007/s10800-016-0970-0.

[23] V.M. Nikolic, S.Lj. Maslovara, G.S. Tasic, T.P. Brdaric, P.Z. Lausevic, B.B. Radak, M. P.M. Kaninski, Kinetics of hydrogen evolution reaction in alkaline electrolysis on a

Ni cathode in the presence of Ni–Co–Mo based ionic activators, Appl. Catal. B: Environ. 179 (2015) 88–94, https://doi.org/10.1016/j.apcatb.2015.05.012.

[24] R.R. Hacha, A.G. Merma, H.J.B. Couto, M.L. Torem, Measurement and analysis of H_2 and O_2 bubbles diameter produced by electroflotation processes in a modified Partridge-Smith cell, Powder Technol 342 (2019) 308–320, https://doi.org/10.1016/j.powtec.2018.09.062.

[25] K.L. Varvaris, D. Esau, F.M. Schuett, T. Jacob, G. Jerkiewicz, Surface structure dependence of electrochemical processes at monocrystalline nickel electrodes. Part 1: the hydrogen evolution reaction, J. Phys. Chem. C 127 (2023) 14711–14722, https://doi.org/10.1021/acs.jpcc.3c01698.

[26] B.E. Conway, L. Bai, H_2 evolution kinetics at high activity Ni-Mo-Cd electrocoated cathodes and its relation to potential dependence of sorption of H, Int. J. Hydrog. Energy 11 (1986) 533–540, https://doi.org/10.1016/0360-3199(86)90020-0.

[27] J.M. Jakšić, M.V. Vojnović, N.V. Krstajić, Kinetic analysis of hydrogen evolution at Ni–Mo alloy electrodes, Electrochim. Acta 45 (2000) 4151–4158, https://doi.org/10.1016/S0013-4686(00)00549-1.

[28] F. Song, X. Hu, Exfoliation of layered double hydroxides for enhanced oxygen evolution catalysis, Nat. Commun. 5 (2014) 4477, https://doi.org/10.1038/ncomms5477.

[29] M.E.G. Lyons, R.L. Doyle, Oxygen evolution at oxidised iron electrodes: a tale of two slopes, Int. J. Electrochem. Sci. 7 (2012) 9488–9501, https://doi.org/10.1016/S1452-3981(23)16213-4.

[30] J M.E. Orazem, B. Tribollet, Time-constant dispersion. Electrochemical Impedance Spectroscopy, 2nd ed., Wiley, Hoboken, NJ, 2017, pp. 319–394, https://doi.org/10.1002/9781119363682.ch13.

[31] T. Pajkossy, Impedance spectroscopy at interfaces of metals and aqueous solutions — Surface roughness, CPE and related issues, Solid State Ionics 176 (2005) 1997–2003, https://doi.org/10.1016/j.ssi.2004.06.023.

[32] E. Barsoukov, J.R. Macdonald (Eds.), Impedance Spectroscopy: Theory, Experiment, and Applications, 2nd ed., John Wiley & Sons, Hoboken, NJ, 2005 https://doi.org/10.1002/9781119381860.

[33] Z. Shiroma, Electrochemical Impedance, Kagaku-Dojin, Kyoto, Japan, 2019, pp. 105–128. ISBN 9784759819915.

[34] M. Takahashi, ζ potential of microbubbles in aqueous solutions: electrical properties of the gas–water interface, J. Phys. Chem. B 109 (2005) 21858–21864, https://doi.org/10.1021/jp0445270.

[35] S. Ke, W. Xiao, N. Quan, Y. Dong, L. Zhang, J. Hu, Formation and stability of bulk nanobubbles in different solutions, Langmuir 35 (2019) 5250–5256, https://doi.org/10.1021/acs.langmuir.9b00144.

[36] R.E. De La Rue, C.W. Tobias, On the conductivity of dispersions, J. Electrochem. Soc. 106 (1959) 827–832, https://doi.org/10.1149/1.2427505.